

Photocapacitor integrating perovskite solar cell and symmetrical supercapacitor generating a conversion storage efficiency over 20 %

Zeyu Song, Jihuai Wu ^{*}, Liuxue Sun, Tingting Zhu, Chunyan Deng, Xiaobing Wang, Guodong Li, Yitian Du, Qi Chen, Weihai Sun, Leqing Fan, Hongwei Chen, Jianming Lin, Zhang Lan

Engineering Research Center of Environment-Friendly Functional Materials, Ministry of Education, Institute of Materials Physical Chemistry, Huaqiao University, Xiamen 361021, Fujian, PR China



ARTICLE INFO

Keywords:
Photocapacitor
Perovskite solar cell
Supercapacitor
Efficiency
Match

ABSTRACT

Solar energy is clean, open, and infinite, but solar radiation on the earth is fluctuating, intermittent, and unstable. So, the sustainable utilization of solar energy needs the complementary combination of high-efficient energy conversion and low-loss energy storage technologies. Hence, a photocapacitor integrated with photo-electrical conversion and electric-chemical storage functions in single device is a cost-effective, volume-effective and functional-effective optimal choice. However, the highest reported conversion storage efficiency of single device is less than 13 %. Here, we investigate the relationship among various efficiencies of photocapacitors during conversion storage process, and propose a function portfolio management concept. Accordingly, a three-terminal photocapacitor integrated with perovskite solar cell and symmetrical supercapacitor units is designed. By harmonizing the energy matching between conversion and storage units and seeking the maximum power points coincide and the maximum efficiency points synchronize, the solar energy conversion storage efficiency of the integrated photocapacitor surpasses milestone of 20 %.

1. Introduction

Affordable, reliable, sustainable and modern energy is a development goal that the United Nations officially adopted in year 2015 [1], clean, open, and infinite solar energy is considered as the most promising strategy to realize this goal [2–4]. Photovoltaic (PV) cells can harvest solar energy and convert it into electricity as long as sunlight is accessible. However, solar radiation on the earth is fluctuating, intermittent, and unstable [5–7]. On the other hand, batteries or supercapacitors can convert electrical energy into chemical energy and store it in the devices. But such energy storage devices are energy-limited closed systems and require constant recharging [8,9]. The complementary combination of high-efficient energy conversion and low-loss energy storage technologies emerges a solar energy conversion and storage integrator, which facilitates the sustainable utilization of renewable energy and is in line with the current trend of multi-function and miniaturization of electronic equipment [5,10–15].

Solar energy conversion and storage integrator concept can be traced back to 1976, when Hodes et al. used polycrystalline CdSe as

photoelectrode, which allowed the storage of the converted energy in situ for subsequent use [16]. In 2004, Miyasaka et al. fabricated a light-driven self-charging capacitor (named as “photocapacitor”) by using a dye-sensitized nanocrystalline film as light absorber [17]. Since then, various solar energy conversion and storage integrators have been developed. The attempted photo-electrical energy conversion units include perovskite, dye-sensitized, organic, quantum dot, silicon, III-V, tandem and other solar cells; the tested electro-chemical energy storage units involve supercapacitors, lithium-ion cells (capacitors), lithium-metal cells, redox flow battery, and so on [10–15, 18–30]. Despite numerous efforts, the multi-function in one device and structural complexity of the integrated device, particularly, the mismatch between energy conversion unit and energy storage unit, lead to relatively low efficiency in the solar energy conversion process and a relatively large energy loss in the energy storage phase. The conversion storage efficiency of the monolithically integrated devices (excluding the solar flow battery and tandem solar cell units) rarely exceed 10 % (Table S1, Supporting Information) [5, 20–23]. and the maximum is 12.43 % [23]. The low conversion storage efficiency of the integrator is

* Correspondence to: Engineering Research Center of Environment-Friendly Functional Materials, Ministry of Education, Huaqiao University, Xiamen 361021, PR China.

E-mail address: jhwu@hqu.edu.cn (J. Wu).

much lower than the power conversion efficiency (PCE) of single PV device [31], which seriously hinder the development of this significant energy device.

In this work, based on the function portfolio management strategy, we clarify the photo-electro-chemical energy conversion process in the integrator. Using perovskite solar cell as energy conversion unit and symmetrical supercapacitor as energy storage unit, an integrated photocapacitor (IPC) is designed. By harmonizing the energy match between the output voltage of the conversion unit and the potential window of the storage unit, seeking their maximum power points coincide and maximum efficiency points synchronize, the solar conversion storage efficiency of the integrated photocapacitor is as high as 20.53 %, which makes this work an important advancement in high-efficient solar conversion and storage integrators.

2. Results and discussion

2.1. Construction of integrated photocapacitors

Perovskite solar cells (PSCs) possess high PCE, open-circuit voltage (V_{OC}), and excellent stability (Table S2). Symmetrical supercapacitors (SSCs) have an appropriate potential window (Table S3) and outstanding charging-discharging features. Based on the function portfolio management strategy and the energy match between the output voltage of the conversion unit and the potential window of the storage unit, we designed a three-terminal integrated photocapacitor (IPC) which was composed of a PSC unit to realize light-to-electrical energy conversion [32,33], an SSC unit to accomplish electric-to-chemical energy storage [8,9], and a Janus electrode to connects the two parts [34]. The PSC unit was fabricated by using $\text{FA}_{0.92}\text{MA}_{0.08}\text{Pb}(\text{I}_{0.92}\text{Br}_{0.08})_3$ (PVK) as photo-active layer, spiro-OMeTAD (Spiro) as hole transport layer (HTL), and titanium oxide (TiO_2) laminated tin oxide (SnO_2) as electron transport layer (ETL); the SSC unit was assembled by using potassium hydroxide (KOH) aqueous solution as electrolyte, and two identical active carbon (AC) as symmetrical electrodes; a copper foil coated with conductive silver paste on both sides was used as the Janus electrode. The schematic architecture diagram of the IPC is shown in Fig. 1a and the actual photos are shown in Fig. S1, and the detailed fabrication procedure is described in Experimental Section.

In the IPCs, the Janus electrode plays a crucial role which is not only used as a support to connect the conversion unit and the storage unit as a monolithic, but also as a sealant to encapsulate PSC and SSC units, avoiding the corrosion of external moisture to PSC and the leakage of internal electrolyte in SSC [35–37]. The IPC features a compact and integrated architecture with three electrical terminals (T1, T2, T3). Under solar irradiation, the light-electric conversion is realized in the PSC unit via connecting T1 and T2; photo-charging is implemented and the converted energy is stored in the SSC unit via connecting T1 and T3 under sunlight; the stored energy in the SSC and the IPC can be applied to the external load (discharging) via connecting T2 with T3, and T1-T3 with T2, respectively. The equivalent circuit in Fig. 1b illustrates the

charging/discharging mode of the IPCs [38,39]. The 3-terminal photocapacitor effectively connects the conversion unit and the storage unit, guarantees charge carriers' smooth transportation, and facilitates the measurement of various photoelectrical parameters.

2.2. Performance of perovskite solar cells

Fig. 2a and b present the structure diagram and the cross-view SEM images of the PSC unit, respectively. From the SEM images, the thickness of the ETL (SnO_2 and/or TiO_2) is about 60–80 nm, the thickness of PVK layer is nearly 600 nm, the thickness of HTL (Spiro) is about 240 nm, the thickness of Au electrode on the hole transport layer is 80 nm, and each interface contact tightly. The orientation of PVK is consistent with that of carrier transport. Large PVK grain is conducive to suppress the carrier non-radiative recombination and enhances the light harvest of PSCs [40].

The photo-generated electrons and holes in the PSC unit are transported by conventional titanium dioxide (TiO_2) and spiro-OMeTAD (Spiro), respectively. However, the different charge carrier mobilities in TiO_2 and Spiro lead to the notorious hysteresis effect, which seriously affects the device efficiency and stability [41,42]. To mitigate the charge carrier accumulation at the interface, a tin oxide (SnO_2) ultrathin layer was deposited on the surface of indium tin oxide (ITO) glass substrate [43]. From Fig. S2, SnO_2 ultrathin layer plays a significant role in alleviating the hysteresis effect. The PSC used SnO_2 or TiO_2 as ETL has higher V_{OC} and FF, thereby has a better PCE than that used SnO_2 or TiO_2 as ETL alone, from the performance statistics of devices shown in Fig. S3.

Fig. 2c presents the photocurrent-voltage ($I-V$) curves of the fabricated PSC and IPC tested under $100 \text{ mW} \cdot \text{cm}^{-2}$ (AM 1.5 G) simulated sunlight irradiation in different scan directions. The photovoltaic metrics, V_{OC} , fill factor (FF), short circuit current density (J_{SC}) and PCE of the devices are listed in Table S4. The optimized PSC exhibits the best performance with $V_{OC} = 1.176 \text{ V}$, $J_{SC} = 23.82 \text{ mA} \cdot \text{cm}^{-2}$ and FF of 0.80, yielding a PCE of 22.44 %. The reverse and forward scan $I-V$ curves of the PSC are almost coincident, and the IPC also has similar behavior, indicating that the hysteresis effects of the PSCs and IPCs are almost negligible after inserting SnO_2 ultrathin layer. From Table S4, the photovoltaic parameters of PSC and IPC are nothing but slightly different, indicating that the PSC has excellent stability. Fig. 2d demonstrates the output current and voltage curves of the PSCs (active area 0.08 cm^2) within 400 s. In a very short time, the output current at 1.00 V reaches the maximum 1.78 mA and the open circuit voltage reaches 1.17 V , respectively, and maintain a stable maximum output, displaying an excellent output stability. These advantages of the PSCs provide a sufficient condition for integrating with SSCs.

2.3. Performance of symmetrical supercapacitors

The symmetric supercapacitor (SSC) based on identical carbon electrode is a typical electric double-layer capacitor, having advantages of stable, safe, inexpensive, and easy processing, which fully meets the

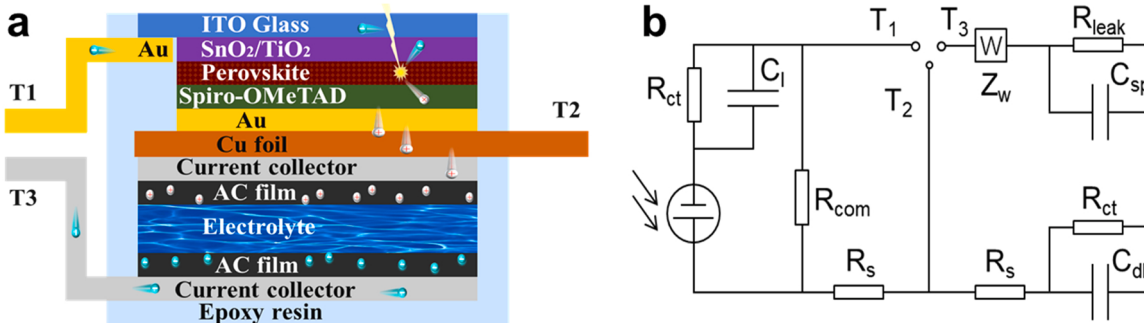


Fig. 1. (a) Structural schematic and (b) Equivalent circuit of the integrated photocapacitor (IPC).

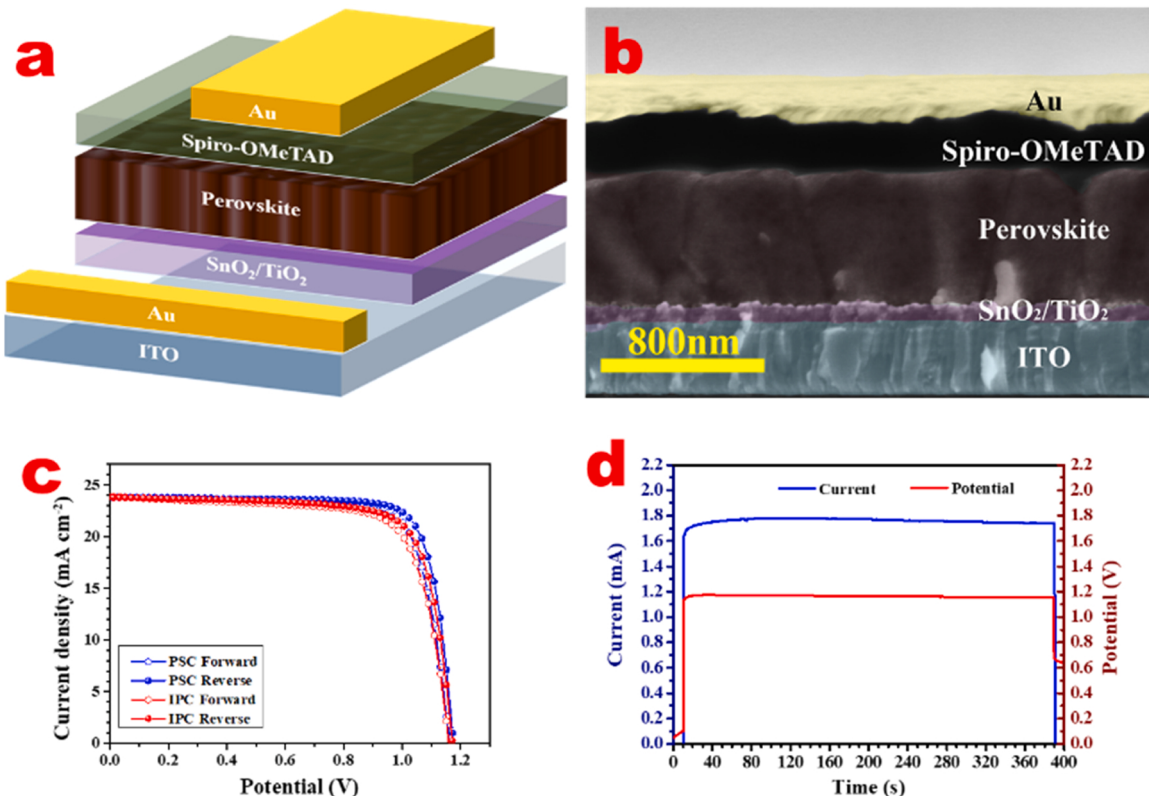


Fig. 2. (a) Structure diagram of PSC units. (b) Cross-view scanning electron microscope (SEM) images of PSC units. (c) Photocurrent-voltage curves of optimized PSCs. (d) Output current and voltage curves of optimized PSCs.

requirements of IPC fabrication. Fig. 3a shows cyclic voltammetry (CV) curves of the SSC with various potential window. Fig. 3b and Fig. S4 show CV curves of the SSC with different sweep speeds. The rectangular-like CV curves at different potential windows and scan rates demonstrate a low internal resistance and stable charge storage in this potential range, indicating quickly and efficiently charging/discharging at the electrode/electrolyte interface [20,44].

Fig. 3c shows the galvanostatic charge-discharge (GCD) curves of the SSCs in various potential windows. Fig. 3d and Fig. S5 displays the GCD curves of the SSCs in different current densities and potential windows. All GCD curves exhibit typical symmetric features with nearly perfect triangular shapes without voltage drop, reflect that the SSCs have ideal charging and discharging performance, indicating an ideal supercapacitor charge storage mechanism in this voltage range with good Joule efficiency [19,45].

From the GCD curves, the Joule efficiency at different potential windows can be calculated by integral area, and the results are shown in Fig. S6. The SSCs have a high Joule efficiency of more than 94 % in a wide potential range, and maintain Joule efficiency exceeding 90 % at a working voltage lower than 0.9 V. Based on the GCD curves, the specific capacitance (C) dependence on the current density is calculated and displayed in Fig. 3e. The C value reaches 61.9 F·g⁻¹ (123.8 mF·cm⁻²) at a low discharge current density of 0.5 A·g⁻¹ (1 mA·cm⁻²). When the discharge current density increases to 4 A·g⁻¹ (8 mA·cm⁻²), the C value is 51.6 F·g⁻¹ (103.2 mF·cm⁻²), only reduced by 16.6 % compared to the current density of 0.5 A·g⁻¹ (1 mA·cm⁻²), indicating high capacitance stability and rate capability [22]. Fig. 3f shows the electrochemical impedance spectroscopy (EIS) curve of the SSCs. The curve consists of a semicircle and a vertical straight line, from which the contact resistance (R_s) of 2.3 Ω and the charge transfer resistance (R_{CT}) of 5.3 Ω can be determined. The imaginary part of the resistance at low frequencies is almost vertical to the real part, indicating a superior capacitive behavior [21]. The above characterizations convincingly demonstrate that the

fabricated SSCs have ideal energy storage performance and offer favorable conditions for integration with PSCs.

2.4. Performance of integrated photocapacitors

At present, there are various understandings and expressions on the photoelectrochemical conversion process for solar conversion and storage integrators [5,10,13–15]. In fact, the energy conversion and storage of the IPCs undergo three processes: light-to-electric energy conversion (photo-charging), electric-to-chemical energy storage, and chemical-to-electric energy output (discharging). Therefore, there are three kinds of efficiencies for single process [η_{L-E} , η_{E-C} , and η_{C-E}] and two kinds of efficiencies for important combination process [$\eta_{CS} = \eta_{L-E-C} = \eta_{L-E} \times \eta_{E-C}$, $\eta_{overall} = \eta_{L-E-C-E} = \eta_{L-E} \times \eta_{E-C} \times \eta_{C-E}$]. The photoelectric conversion efficiency (η_{L-E}) mainly depends on the virtue of the PSCs, and the Joule efficiency (η_{C-E}) mainly relies on the merits of the SSCs. The η_{E-C} is determined by the synergetic effect and the matching degree of the PSCs and SSCs. The detailed measurement procedures and calculation of various efficiencies are shown in Experimental Section.

Fig. 4a shows the current-voltage ($I-V$) curves of the PSC and IPC during photo-charging. The PSC obtains a light-to-electric conversion efficiency (η_{L-E}) of 22.44 % at maximum power point (MPP) of 1.010 V, while the IPC obtains a solar conversion storage efficiency (η_{CS} , η_{L-E-C}) of 20.53 % at MPP of 0.944 V. The MPP values of PSC and IPC are very close, at 1.010 V and 0.944 V, respectively, implying little energy loss in the integrating between the PSC and SSC, which is a significant symbol of the perfect match between SSC and PSC in IPC. Interestingly, in the beginning of photo-charging with a voltage range of 0–0.1 V, the IPC generates a larger current density than that of PSC, which may be attributed to the rapid formation of electric double-layer in SSCs.

Fig. 4b shows the efficiency-voltage ($E-V$) curves of the IPC during photo-charging. IPC achieves a maximum conversion storage efficiency (η_{CS}) of 20.53 % at 0.944 V (maximum efficiency point, MEP), and an

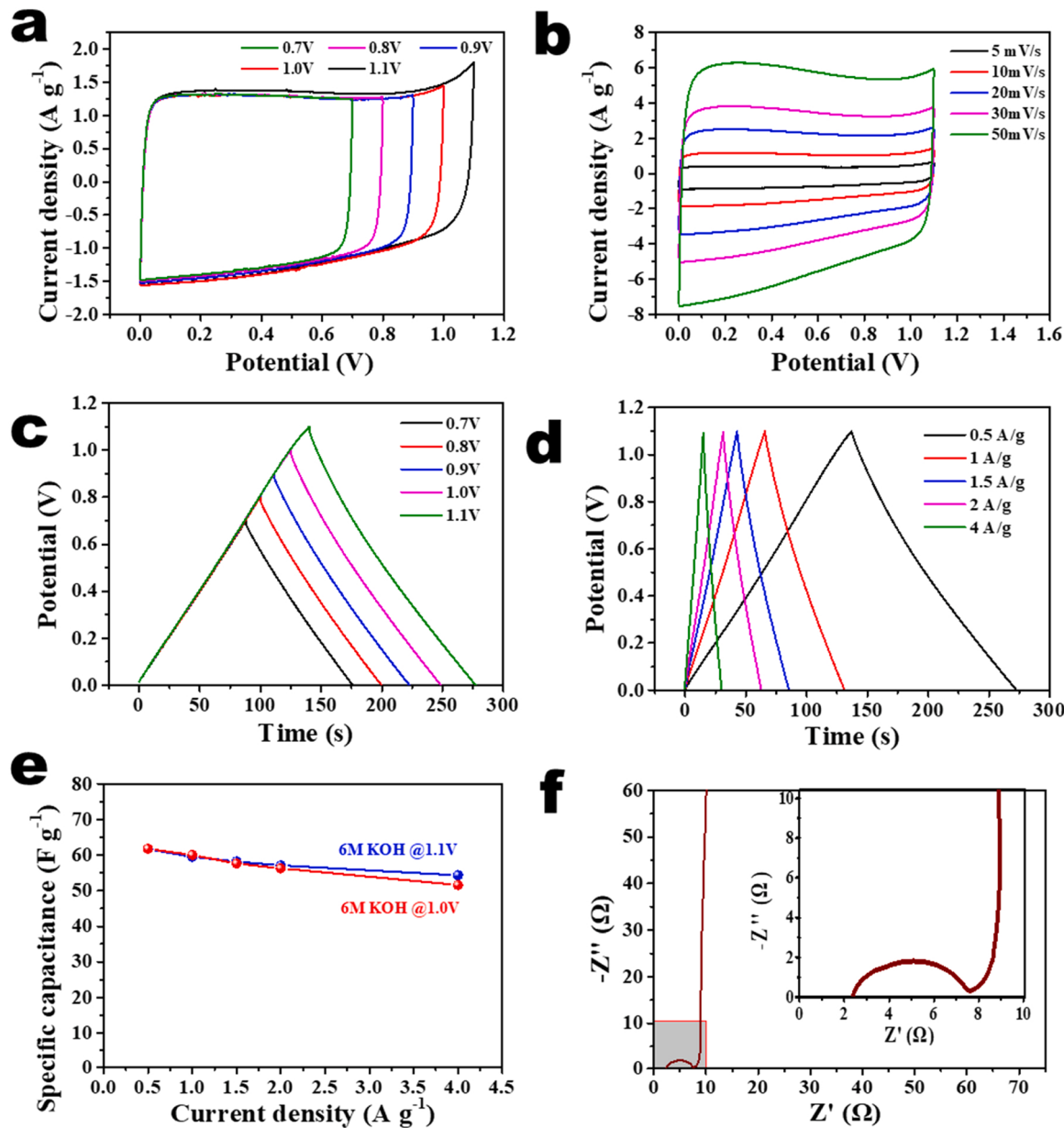


Fig. 3. Performance of the SSC with structure of AC//KOH(6 M)//AC (AC mass: 4 mg). (a) CV curves in various potential window at a sweep speed of 10 $\text{mA} \cdot \text{s}^{-1}$. (b) CV curves in various sweep speeds at potential window of 0–1.1 V. (c) GCD curves in different potential window at a current density of 0.5 A g^{-1} . (d) GCD curves in different current densities at the potential window of 1.1 V. (e) Specific capacitances in different current densities at the potential window of 1.0 V and 1.1 V. (f) EIS curve of SSCs. The insert is locality zoom and equivalent circuit.

appropriate η_{C-E} of 90 % at 0.913 V. Therefore, the IPC achieves a maximum overall efficiency ($\eta_{overall}$) of 18.34 % at 0.919 V. The efficiency values of 20.53 % and 18.34 % obtained by us are higher than the present record conversion storage efficiency and overall efficiency of any other solar-charging integrated devices. As shown in Fig. 4b, the potential values of various MEPs are very close, which is the direct reason for the high conversion store efficiency and overall efficiency. Furthermore, if the potential values of various MEPs coincide completely, the theoretical maximum η_{CS} and $\eta_{overall}$ can be obtained. This is the core concept of the function portfolio management strategy proposed by us.

The temporal charging profile (Fig. 4c) demonstrates both the dynamic change in photocurrent and voltage of the IPCs as a function of charging time. In the early period of solar illumination, voltage increases linearly with time, displaying a similar behavior as the SSC does in galvanostatic charge; meanwhile, the current is almost unchanged. After

the voltage rising to 0.9 V, the voltage slowly increases and finally stabilizes at 1.1 V, which is close to the V_{OC} value of the PSCs. At the same time, the current density decreases gradually and remains at about 0.4 $\text{mA} \cdot \text{cm}^{-2}$ after 150 s of light illumination. The decrease of current density is due to the gradual saturation of the SSC charging and the decline of real power output of the solar cell when the operation voltage approaches the V_{OC} [22,45].

Fig. 4d shows the efficiency change of the IPC with time during photo-charging. Evident from this plot, η_{C-E} increases with time and reaches the maximum value of 96 % at 34.6 s; and then the efficiency slowly decreases to 90 % at 103.8 s, and rapidly decreases after 120 s. The η_{L-E-C} increases with time and reaches the maximum value of 20.53 % at 108.3 s, and the corresponding energy storage efficiency (η_{E-C}) is up to 88.88 %. The time points for two maximum efficiencies are not synchronized. Based on $\eta_{overall} = \eta_{L-E-C} \times \eta_{C-E}$, the $\eta_{overall}$ obtains the maximum value of 18.34 % at 104.8 s. Searching for the synchronous

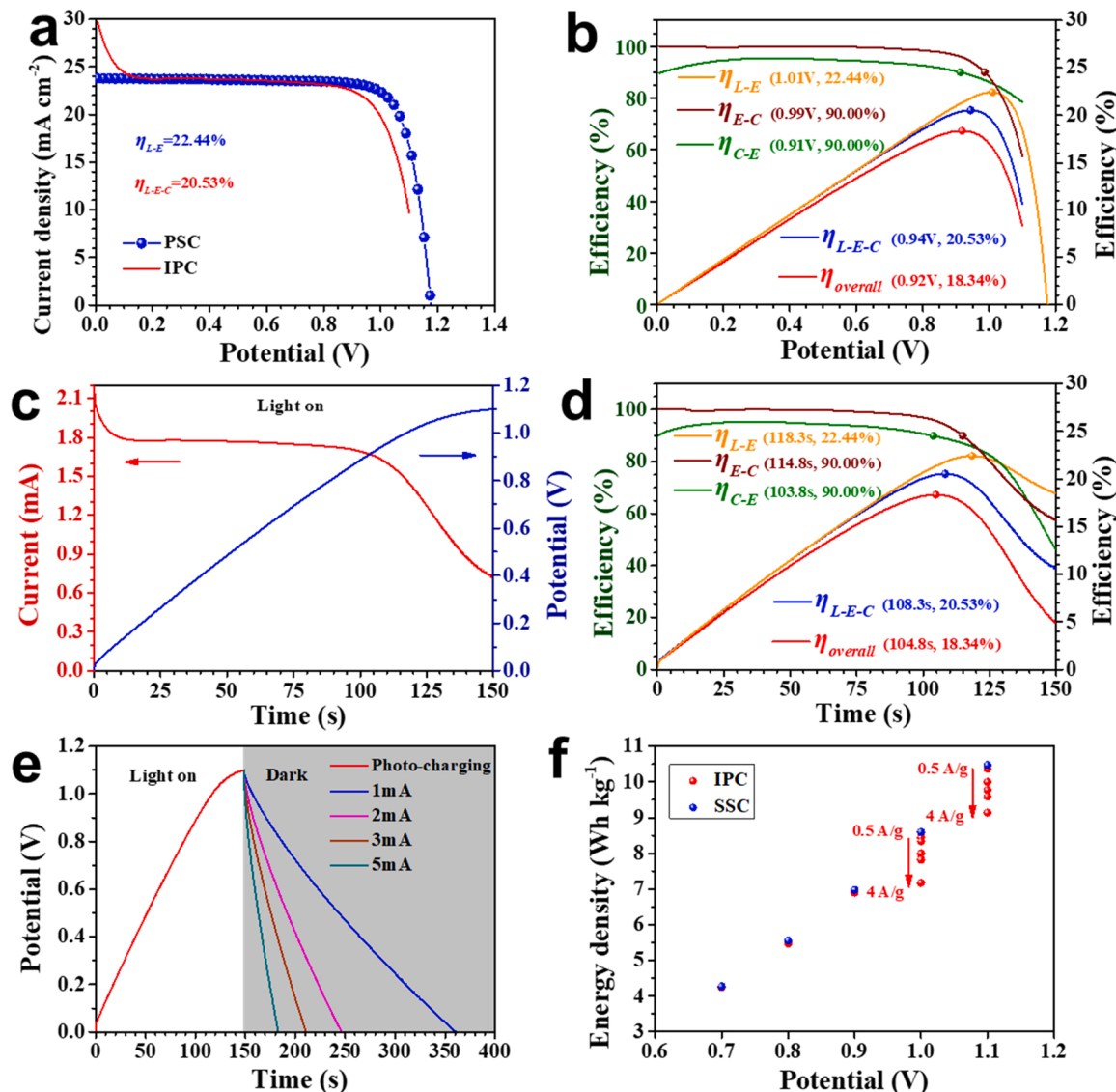


Fig. 4. (a) Photo-charging current-voltage curves of PSC and IPC. (b) Efficiency-voltage curves of IPC. (c) Photovoltage-time and photocurrent-time profiles of IPCs during photo-charging. (d) Efficiency-time profiles of the IPCs during photo-charging. (e) Photo-charging (white sections) and galvanostatic-discharge (gray sections) curves of IPCs at different discharge current densities. (f) Energy densities of the SSCs and IPCs at different voltage windows in galvanostatic discharge.

MEPs is the key to obtain the maximum $\eta_{overall}$.

To investigate the ability of the IPC to harvest solar energy and deliver energy, we measured the photo-charging and galvanostatic-discharge curves of IPCs at different discharge current densities (Fig. 4e) and different potential windows (Fig. S7). From Fig. 4e, after 150 s photo-charging under one sun illumination, the voltage of the IPC increases to about 1.1 V (the V_{OC} of PSC and the potential window of SSC), and the photo-charging of the SSC is close to saturation [22]. The IPC is subsequently galvanostatically discharged at current of 1, 2, 3, and 5 mA in the dark, taking 211.5, 97.3, 61.7, and 33.9 s to complete discharge.

The discharge performance of the IPCs is almost the same as that of the SSCs. The energy densities of the IPCs and the SSCs in different potential windows are shown in Fig. 4f. Under the potential window of 1.0 V and discharge power densities of 500, 1000, 1500, 2000, and 4000 W·kg⁻¹, the IPC has energy densities of 8.44, 8.33, 8.00, 7.82, and 7.17 Wh·kg⁻¹, respectively. When the discharge current density is 0.5 mA·cm⁻², the energy density is 16.88 µWh·cm⁻². Under the maximum potential window of 1.1 V and discharge power density of 550 W·kg⁻¹ (2.2 mW·cm⁻²), the IPC has an energy density of

10.17 Wh·kg⁻¹ (20.34 µWh·cm⁻²), slightly smaller than that of the SSC (10.47 Wh·kg⁻¹, 20.94 µWh·cm⁻²). Under the window potentials of 0.7, 0.8, 0.9, and 1.0 V, IPC has energy densities of 4.25, 5.47, 6.90, and 8.44 Wh·kg⁻¹, respectively, which is slightly smaller than those of the SSCs (4.27, 5.55, 6.98, and 8.60 Wh·kg⁻¹). The slight difference in energy density between IPCs and SSCs demonstrates that the characteristics of the SSC are preserved, but not discounted by device integration. The high energy density of IPCs and SSCs obtained in the broad voltage window of 1.1 V indicate that the voltage window plays a vital role in determining the performance of devices [41]. Benefited from the high V_{OC} (~1.10 V) of the PSC unit, the photo-charging voltage of IPCs is well optimized.

Cycling stability of IPCs was tested by photo-charging and galvanostatic-discharging at a current density of 0.5 A·g⁻¹ for 200 cycles (Fig. 5a). Both the capacitance and the overall efficiency show a trend of slightly increasing to a maximum value from the 50th cycle to the 100th cycle and then slowly decreasing. Even after 200 cycles, the overall efficiency still retains 98.5 % of the maximum value, indicating a superior stability of IPCs. This is benefited from the outstanding cycling performance of SSCs, as shown in Fig. 5b. The Coulombic efficiencies of

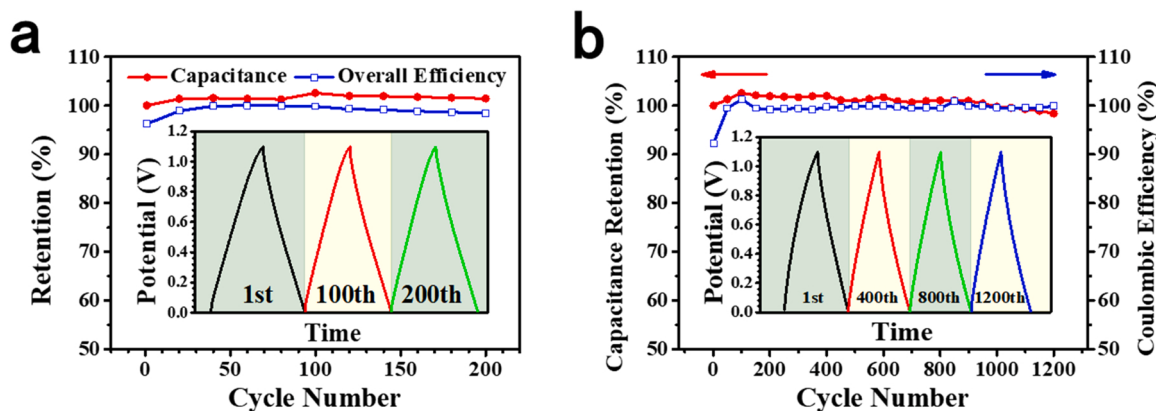


Fig. 5. (a) Photo-charging and galvanostatic-discharge cycling stability of IPCs (AC mass: 4 mg) for 200 cycles. (b) Capacitance stability and Coulombic efficiency of supercapacitor (AC mass: 4 mg) measured by the galvanostatic charge/discharge test at current density of $1 \text{ A}\cdot\text{g}^{-1}$ for 1200 cycles.

the SSCs increase from 92 % to ~ 100 % in the first 50 cycles for activation, and a similar increase in capacitance. After 1200 cycles, the capacitance retained 98.4 % of the initial value and the Coulombic efficiency remains at ~ 100 %.

3. Conclusions

In summary, we have demonstrated a new strategy for realizing function harmonized photocapacitors that simultaneously achieve high-effective solar conversion and low-loss energy storage. Our design of a 3-terminal integrated structure alleviates the internal and external instability factors and guarantees charge carriers' smooth transportation. The rational energy match between PSCs and SSCs improves the combination efficiency, and the coordination of power points and efficiency points decrease the energy loss. These effects enabled us to realize a record conversion storage efficiency exceeding 20 %. At the same time, it has superior cycling stability, even after 200 photo-charge and galvanostatic-discharge cycles, the overall efficiency has almost no attenuation. The integrated PV-storage system is still in the early research stage [5]. Improvements in device stability demands quasi-solid, solid or ionic liquid electrolytes [45]. Amelioration in device energy density might be realized by using high energy storage units, like Li-ion capacitors [5,27].

4. Experimental and method

4.1. Materials

Tin oxide (15 wt% colloidal dispersion in water), 2,2',7,7'-tetrakis [N,N-di(4-methoxyphenyl) amino]-9,9'-spirobifluorene (spiro-OMeTAD) (99.0 %), acetylene black (99.9 %), lead bromide (99.999 %), formamidine hydroiodide (98.0 %), methylamine hydrobromide (98 %) and methylamine hydrochloride (99.0 %) were purchased from Alfa Aesar. Lead iodide (99.99 %) was purchased from TCI. Titanium tetrachloride (AR, 99.0 %), ethanol (ACS, 99.7 %), benzyl alcohol (ACS, 99.0 %), potassium hydroxide (95 %) and polytetrafluoroethylene (60 wt%) were purchased from Aladdin. Bis(trifluoromethane)sulfonimide lithium salt (LiTFSI) (99.95 %), 4-tert-butylpyridine (98 %), acetonitrile (anhydrous, 99.8 %), dimethylformamide (DMF) (anhydrous, 99.8 %), dimethyl sulfoxide (DMSO) (anhydrous, ≥ 99.9 %) and chlorobenzene (CB) (anhydrous, 99.5%) were purchased from Sigma-Aldrich. Ethyl ether (AR, 99.7 %), methanol (AR, 99.5 %), trichloromethane (AR, 99.0 %), acetone (ACS, 99.5 %) and charcoal activated powder (99.0 %) were purchased from Sinopharm Chemical Reagent Co., Ltd. Phenolic epoxy resin (3 M) were purchased from DuPont de Nemours, USA. ECA-1001 conductive silver paste and 0.03 mm thick copper foil were purchased directly. All materials were used as received without further processing.

4.2. Fabrication of PSC solar cells

TiO₂ nanocrystals are used as electron transport layer. The specific synthesis method refers to the work of Tu et al. [46]. The obtained TiO₂ nanocrystals were dispersed in anhydrous chloroform and methanol (volume ratio 1:1) to obtain a TiO₂ colloidal solution ($\sim 5 \text{ mg}\cdot\text{mL}^{-1}$) for later use.

The pre-patterned indium tin oxide (ITO) substrates (Ying Kou You Xuan Trade Co., Ltd., $10 \Omega\cdot\text{sq}^{-1}$) were cleaned with acetone, ethanol, and ultrapure water under ultrasound for 20 min. Followed by ozone treatment for 30 min. SnO₂ colloidal solution (diluted with ultrapure water to 3 wt%) was spin-coated at 3500 rpm for 20 s on the ITO, and then annealed at 180 °C for 30 min. After cooling to room temperature, the prepared TiO₂ colloidal solution was spin-coated at 4000 rpm for 20 s on the SnO₂ layer, and then annealed at 180 °C for 3 min. The deposition of TiO₂ was repeated for several times to meet the thickness requirements. The perovskite (PVK) precursor was a mixed solution of 1.47 M PbI₂, 0.11 M PbBr₂, 1.4 M FAI, 0.11 M MABr and 0.5 M MACl dissolved in DMSO/DMF solvent (volume ratio of 1/6). The perovskite film was deposited on the TiO₂ layer by an anti-solvent spin-coating process. The PVK precursor solution was spin-coated on the TiO₂ layer, firstly at 1000 rpm for 10 s, then at 6000 rpm for 20 s, and drop 140 μL of chlorobenzene on the rotating substrate at 5 s before the end of spin coating. The resultant film was annealed on a heating stage at 100 °C for 45 min. After cooling, a chlorobenzene solution containing spiro-OMeTAD (72.3 $\text{mg}\cdot\text{mL}^{-1}$), 4-tert-butylpyridine (28.8 $\mu\text{L}\cdot\text{mL}^{-1}$) and LiTFSI salt solution (17.5 μL , 170 $\text{mg}\cdot\text{mL}^{-1}$ dissolved in acetonitrile) as hole transport layer was spin-coated at 4000 rpm on the perovskite film. Finally, 80 nm gold as counter electrode was deposited on spiro-OMeTAD under vacuum. A planer perovskite solar cell (PSC) with architecture of ITO/SnO₂/TiO₂/FA_{0.92}MA_{0.08}Pb(I_{0.92}Br_{0.08})₃/spiro-OMeTAD/Au and light active area of 0.08 cm^2 was thus fabricated.

4.3. Fabrication of supercapacitors

Activated charcoal: acetylene black: polytetrafluoroethylene with mass ratio of 8:1:1 were mixed and dispersed in absolute ethanol, ultrasonically treated for 15 min, and then stirred to form an active carbon (AC) paste. The AC paste was pressed into a film with a roll press at 0.5 MPa, and then dried in a vacuum oven at 70 °C overnight. Two identical AC films were pressed into a 200-mesh stainless steel net and used as symmetric electrodes of supercapacitor. An epoxy resin was used to fix the two symmetric electrodes face to face and separate a gap of 1 mm. After curing, a 6 M KOH aqueous solution was used as electrolyte to fill the gap and then the device was sealed. Thus, a symmetrical supercapacitor (SSC) with architecture of AC//KOH(6 M)//AC was fabricated (AC mass: 2 mg or 4 mg).

4.4. Fabrication of integrated photocapacitors

The conductive silver paste is coated as thinly as possible on both sides of the copper foil with a glass sheet to make Janus electrodes. The Au electrode of PSC and the current collector of SSC are stacked on both sides of the Janus electrode, respectively. Then, the PSC unit and SSC unit were placed in a home-made mold, epoxy resin was filled and cured at 75 °C for 30 min to obtain an integrated photocapacitor (IPC) device. Fig. 1a presents a device architecture of the IPC composed of an SSC unit and a PSC unit.

4.5. Characterizations

The morphologies characterizations were performed on the field emission scanning electron microscopy (FE-SEM, SU8010, Hitachi). The photocurrent density-voltage (J-V) characteristic curve of PSCs and IPCs were recorded with a Keithley 2420 source-measure unit under 100 mW·cm⁻² (AM 1.5 G) illumination provided by a solar light simulator (Newport Oriel Sol 3 A class, USA, calibrated by a Newport reference cell). The steady-state output performance of PSCs, the electrochemical performance of devices was measured by electrochemical workstation (CHI660E, Chenghua Co. Ltd. Shanghai).

T1 and T2 were two electrodes for pristine PSC test. T3 and T2 were two electrodes for SSC test. T1-T3 and T2 were two electrodes for IPC test. The incident light of photo-charging was provided by a solar light simulator with intensity of 100 mW·cm⁻² (AM 1.5 G). The discharging test was carried out under dark and outputs a constant current. The photo-charge and discharge curves were recorded by the electrochemical workstation.

4.6. Calculations

There are three kinds of efficiencies for single process [η_{L-E} , η_{E-C} , and η_{C-E}] and three kinds of efficiencies for combination process [$\eta_{CS} = \eta_{L-E-C} = \eta_{L-E} \times \eta_{E-C}$, $\eta_{overall} = \eta_{L-E-C-E} = \eta_{L-E} \times \eta_{E-C} \times \eta_{C-E}$]. These efficiencies are defined and calculated based on the following formula:

- 1) Light-to-electric energy conversion efficiency (η_{L-E}) of the device is calculated:

$$\eta_{L-E} = E_{out}/E_{in} \times 100 \% \quad (1)$$

$$E_{in} = P_{in} \times S_{PSC} \times (t2 - t1)$$

where E_{in} and E_{out} are the light energy (mW·s) received by the PSC during the light charging time period ($t1$ to $t2$) (s) and the output energy converted into electrical energy (mW·s), respectively. Among them, P_{in} and S_{PSC} are the incident light power density (mW cm⁻²) and effective light area (cm²). E_{out} is calculated by integrating the output current I_{out} (mA) and V_{out} (V) in the light charging section.

- 2) Electric-to-chemical energy storage efficiency (η_{E-C}) for PSC photo-charge to SSC:

$$\eta_{E-C} = E_c/E_{out} \times 100 \% \quad (2)$$

where E_c is the charge energy (mW·s) of the PSC stored in the SCC in the light charging section.

- 3) Joule efficiency (η_{Joule} , η_{E-C-E}) of IPCs for galvanostatically charging with Land machine as power supply:

$$\eta_{Joule} = \eta_{E-C-E} = E_d/E_c \times 100 \% \quad (3)$$

where E_c and E_d are the charge and discharge energy (mW·s), E_c is calculated by integrating the charge current I_c (mA) and V_c (V) in the light charging section, while E_d is calculated by integrating the

discharge current I_d (mA) and V_d (V) in the discharging section.

- 4) Conversion-storage efficiency (η_{CS}) of IPCs:

$$\eta_{CS} = \eta_{L-E-C} = \eta_{L-E} \times \eta_{E-C} = E_c/E_{in} \times 100 \% \quad (4)$$

- 5) Overall efficiency ($\eta_{overall}$) of IPCs:

$$\eta_{overall} = \eta_{L-E-C-E} = \eta_{L-E} \times \eta_{E-C} \times \eta_{C-E} = E_d/(P_{in} \times S_{PSC} \times \Delta t) \times 100 \% \quad (5)$$

CRediT authorship contribution statement

Zeyu Song conceived the idea, performed mostly experiments and wrote the first draft. **Jihuai Wu** conceived the idea, supervised the research, provided funding for the work and wrote the final manuscript. **Liuxue Sun** participated in photocapacitor research. **Tingting Zhu** carried out partly research on supercapacitors. **Chunyan Deng**, **Xiaobing Wang**, and **Guodong Li** mainly participated in solar cell research. **Yitian Du** and **Qi Chen** verified the experimental results. **Weihai Sun** participated in photocapacitor research. **Leqing Fan**, **Hongwei Chen**, and **Jianming Lin** carried out research on supercapacitors. **Zhan Lan** implemented project administration. All authors discussed the results and commented on the manuscript.

Declaration of Competing Interest

The authors declare that they have no known competing financial interests or personal relationships that could have appeared to influence the work reported in this paper.

Acknowledgements

The authors are grateful to the financial support from the National Natural Science Foundation of China (Nos. 51972123, U1705256, 61804058).

Appendix A. Supporting information

Supplementary data associated with this article can be found in the online version at doi:10.1016/j.nanoen.2022.107501.

References

- [1] United Nations General Assembly, Transforming Our World: the 2030 Agenda for Sustainable Development. (<http://sustainabledevelopment.un.org/post2015/transformingourworld>). 2021 (Accessed 26 July 2021).
- [2] N. Lewis, Research opportunities to advance solar energy utilization, *Science* 351 (2016) aad1920.
- [3] S. Chu, Y. Cui, N. Liu, The path towards sustainable energy, *Nat. Mater.* 16 (2017) 16–22.
- [4] J. Montoya, L. Seitz, P. Chakrhanont, A. Vojvodic, T. Jaramillo, J. Nørskov, Materials for solar fuels and chemicals, *Nat. Mater.* 16 (2017) 70–81.
- [5] A. Gurung, Q. Qiao, Solar charging batteries: advances, challenges, and opportunities, *Joule* 2 (2018) 1217–1230.
- [6] Z. Yang, J. Zhang, M. Kintner-Meyer, X. Lu, D. Choi, J. Lemmon, J. Liu, Electrochemical energy storage for green grid, *Chem. Rev.* 111 (2011) 3577–3613.
- [7] J. Wu, Z. Lan, J. Lin, M. Huang, Y. Huang, L. Fan, G. Luo, Y. Lin, Y. Xie, Y. Wei, Counter electrodes in dye-sensitized solar cells, *Chem. Soc. Rev.* 46 (2017) 5975–6023.
- [8] P. Simon, Y. Gogotsi, B. Dunn, Where do batteries end and supercapacitors begin? *Science* 343 (2014) 1210–1211.
- [9] P. Simon, Y. Gogotsi, Materials for electrochemical capacitors, *Nat. Mater.* 7 (2008) 845–854.
- [10] W. Li, J. Zheng, B. Hu, H. Fu, M. Hu, A. Veyssal, Y. Zhao, J. He, T. Liu, A. Ho-Bailie, S. Jin, High-performance solar flow battery powered by a perovskite/silicon tandem solar cell, *Nat. Mater.* 19 (2020) 1326–1331.
- [11] A. Gurung, K. Reza, S. Mabrouk, B. Bahrami, R. Pathak, B. Lamsal, S. Rahman, N. Ghimire, R. Bobba, K. Chen, J. Pokharel, A. Baniya, M. Laskar, M. Liang, W. Zhang, W. Zhang, S. Yang, K. Xu, Q. Qiao, Rear-illuminated perovskite photorechargeable lithium battery, *Adv. Funct. Mater.* 30 (2020) 2001865.
- [12] W. Li, H. Fu, Y. Zhao, J. He, S. Jin, 14.1% efficient monolithically integrated solar flow battery, *Chem* 4 (2018) 2644–2657.

- [13] B. Lu, F. Liu, G. Sun, J. Gao, T. Xu, Y. Xiao, C. Shao, X. Jin, H. Yang, Y. Zhao, Z. Zhang, L. Jiang, L. Qu, Compact assembly and programmable integration of supercapacitors, *Adv. Mater.* 32 (2020) 1907005.
- [14] M. Sygletou, C. Petridis, E. Kymakis, E. Stratakis, Advanced photonic processes for photovoltaic and energy storage systems, *Adv. Mater.* 29 (2017) 1700335.
- [15] V. Vega-Garita, L. Ramirez-Elizondo, N. Narayan, P. Bauer, Integrating a photovoltaic storage system in one device: a critical review, *Prog. Photovolt.* 27 (2019) 346–370.
- [16] G. Hodes, J. Manassen, D. Cahen, Photoelectrochemical energy conversion and storage using polycrystalline chalcogenide electrodes, *Nature* 261 (1976) 403–404.
- [17] T. Miyasaka, T. Murakami, The photocapacitor: an efficient self-charging capacitor for direct storage of solar energy, *Appl. Phys. Lett.* 85 (2004) 3932–3934.
- [18] Z. Tian, Z. Sun, Y. Shao, L. Gao, R. Huang, Y. Shao, R. Kaner, J. Sun, Ultrafast rechargeable Zn micro-batteries endowing a wearable solar charging system with high overall efficiency, *Energy Environ. Sci.* 14 (2021) 1602–1611.
- [19] Z. Tian, X. Tong, G. Sheng, Y. Shao, L. Yu, V. Tung, J. Sun, R. Kaner, Z. Liu, Printable magnesium ion quasi-solid-state asymmetric supercapacitors for flexible solar-charging integrated units, *Nat. Commun.* 10 (2019) 4913.
- [20] X. Xu, S. Li, H. Zhang, Y. Shen, S. Zakeeruddin, M. Graetzel, Y. Cheng, M. Wang, A power pack based on organometallic perovskite solar cell and supercapacitor, *ACS Nano* 9 (2015) 1782–1787.
- [21] R. Liu, J. Wang, T. Sun, M. Wang, C. Wu, H. Zou, T. Song, X. Zhang, S. Lee, Z. Wang, B. Sun, Silicon nanowire/polymer hybrid solar cell-supercapacitor: a self-charging power unit with a total efficiency of 10.5%, *Nano Lett.* 17 (2017) 4240–4247.
- [22] J. Kim, S. Lee, Y. Hwang, S. Lee, B. Park, J. Jang, K. Lee, A highly efficient self-power pack system integrating supercapacitors and photovoltaics with an area-saving monolithic architecture, *J. Mater. Chem. A* 5 (2017) 1906–1912.
- [23] T. Zhu, Y. Yang, Y. Liu, R. Lopez-Hallman, Z. Ma, L. Liu, X. Gong, Wireless portable light-weight self-charging power packs by perovskite-organic tandem solar cells integrated with solid-state asymmetric supercapacitors, *Nano Energy* 78 (2020), 105397.
- [24] T. Gibson, N. Kelly, Solar photovoltaic charging of lithium-ion batteries, *J. Power Sources* 195 (2010) 3928–3932.
- [25] Z. Yang, L. Li, Y. Luo, R. He, L. Qiu, H. Lin, H. Peng, An integrated device for both photoelectric conversion and energy storage based on free-standing and aligned carbon nanotube film, *J. Mater. Chem. A* 1 (2013) 954–958.
- [26] J. Xu, Y. Chen, L. Dai, Efficiently photo-charging lithium-ion battery by perovskite solar cell, *Nat. Commun.* 6 (2015) 8103.
- [27] A. Gurung, K. Chen, R. Khan, S. Abdulkarim, G. Varnekar, R. Pathak, R. Naderi, Q. Qiao, Highly efficient perovskite solar cell photocharging of lithium ion battery using DC-DC booster, *Adv. Energy Mater.* 7 (2017) 1602105.
- [28] J. Liang, G. Zhu, C. Wang, P. Zhao, Y. Wang, Y. Hu, L. Ma, Z. Tie, J. Liu, Z. Jin, An all-inorganic perovskite solar capacitor for efficient and stable spontaneous photocharging, *Nano Energy* 52 (2018) 239–245.
- [29] C. Li, S. Cong, Z. Tian, Y. Song, L. Yu, C. Lu, Y. Shao, J. Li, G. Zou, M. Rummeli, S. Dou, J. Sun, Z. Liu, Flexible perovskite solar cell-driven photo-rechargeable lithium-ion capacitor for self-powered wearable strain sensors, *Nano Energy* 60 (2019) 247–256.
- [30] X. Liu, Y. Wang, X. Cui, M. Zhang, B. Wang, M. Rager, Z. Shu, Y. Yang, Z. Li, Z. Lin, Enabling highly efficient photocatalytic hydrogen generation and organics degradation via a perovskite solar cell-assisted semiconducting nanocomposite photoanode, *J. Mater. Chem. A* 7 (2019) 165–171.
- [31] NREL, Best Research-cell Efficiencies Chart. (<https://www.nrel.gov/pv/cell-efficiency.html>), 2022 (Accessed 26 January 2022).
- [32] W. Yang, J. Noh, N. Jeon, Y. Kim, S. Ryu, J. Seo, S. Seok, High-performance photovoltaic perovskite layers fabricated through intramolecular exchange, *Science* 348 (2015) 1234–1237.
- [33] M. Lee, J. Teusche, T. Miyasaka, T. Murakami, H. Snaith, Efficient hybrid solar cells based on meso-superstructured organometal halide perovskites, *Science* 338 (2012) 643–647.
- [34] P. Chen, T. Li, G. Li, X. Gao, Quasi-solid-state solar rechargeable capacitors based on in-situ Janus modified electrode for solar energy multiplication effect, *Sci. China Mater.* 63 (2020) 1693–1702.
- [35] F. Bella, G. Griffini, J. Correa-Baena, G. Saracco, M. Gratzel, A. Hagfeldt, S. Turri, C. Gerbaldi, Improving efficiency and stability of perovskite solar cells with photocurable fluoropolymers, *Science* 354 (2016) 203–206.
- [36] J. Wu, Z. Lan, J. Lin, M. Huang, Y. Huang, L. Fan, G. Luo, Electrolytes in dye-sensitized solar cells, *Chem. Rev.* 115 (2015) 2136–2173.
- [37] M. Zhang, Z. Lin, Monolithic perovskite solar capacitor enabled by double-sided TiO₂ nanotube arrays, *ACS Energy Lett.* 7 (2022) 1260–1265.
- [38] S. Intermitte, C. Arizzani, F. Soavi, S. Gholipour, S. Turren-Cruz, J. Correa-Baena, M. Saliba, N. Vlachopoulos, A. Morteza Ali, A. Hagfeldt, M. Gratzel, Perovskite solar cell-electrochemical double layer capacitor interplay, *Electrochim. Acta* 258 (2017) 825–833.
- [39] A. Roy, P. Majumdar, P. Sengupta, S. Kundu, S. Shinde, A. Jha, K. Pramanik, H. Saha, A photoelectrochemical supercapacitor based on a single BiVO₄-RGO bilayer photocapacitive electrode, *Electrochim. Acta* 329 (2020), 135170.
- [40] B. Yang, O. Dyck, J. Poplawsky, J. Keum, A. Puretzky, S. Das, I. Ivanov, C. Rouleau, G. Duscher, D. Geohagan, K. Xiao, Perovskite solar cells with near 100% internal quantum efficiency based on large single crystalline grains and vertical bulk heterojunctions, *J. Am. Chem. Soc.* 137 (2015) 9210–9213.
- [41] H. Snaith, A. Abate, J. Ball, G. Eperon, T. Leijten, N. Noel, S. Stranks, J. Wang, K. Wojciechowski, W. Zhang, Anomalous hysteresis in perovskite solar cells, *J. Phys. Chem. Lett.* 5 (2014) 1511–1515.
- [42] P. Liu, W. Wang, S. Liu, H. Yang, Z. Shao, Fundamental understanding of photocurrent hysteresis in perovskite solar cells, *Adv. Energy Mater.* 9 (2019) 1803017.
- [43] Q. Guo, J. Wu, Y. Yang, X. Liu, Z. Lan, J. Lin, M. Huang, Y. Wei, J. Dong, J. Jia, Y. Huang, High-performance and hysteresis-free perovskite solar cells based on rare-earth-doped SnO₂ mesoporous scaffold, *Research* 2019 (2019) 4049793.
- [44] C. Gao, J. Huang, Y. Xiao, G. Zhang, C. Dai, Z. Li, Y. Zhao, L. Jiang, L. Qu, A seamlessly integrated device of micro-supercapacitor and wireless charging with ultrahigh energy density and capacitance, *Nat. Commun.* 12 (2021) 2647.
- [45] A. Cohn, W. Erwin, K. Share, L. Oakes, A. Westover, R. Carter, R. Bardhan, C. Pint, All silicon electrode photocapacitor for integrated energy storage and conversion, *Nano Lett.* 15 (2015) 2727–2731.
- [46] Y. Tu, J. Wu, M. Zheng, J. Huo, P. Zhou, Z. Lan, J. Lin, M. Huang, TiO₂ quantum dots as superb compact block layers for high-performance CH₃NH₃PbI₃ perovskite solar cells with an efficiency of 16.97%, *Nanoscale* 7 (2015) 20539–20546.